Upconversion optical fiber microsphere sensor designed for precise measurement of FPGA temperature

MIAO YU,[1,†] XIAOLEI HAO,[1,†] SHAOSHUAI HAN,[1] DUO WANG,[1] SHANSHAN ZHANG,[1] MENGXIAO LI,[1] PEIYAO AN,[1] DI LIAN,[1] MINGXIANG YANG,[1] RENSHENG SHEN,[2] XIN YANG,[3,4] AND ZHENLIN WU[1,5]

[1]*School of Optoelectronic Engineering and Instrumentation Science, Dalian University of Technology, Dalian 116024, China*
[2]*School of Integrated Circuits, Dalian University of Technology, Dalian 116024, China*
[3]*Department of Electrical and Electronic Engineering, School of Engineering, Cardiff University, Cardiff CF24 3AA, UK*
[4]*yangx26@cardiff.ac.uk*
[5]*zhenlinwu@dlut.edu.cn*
[†]These authors contributed equally.

Abstract: In the realm of field-programmable gate array (FPGA) design, temperature emerges as a pivotal parameter that critically impacts system stability, reliability, energy efficiency, and fault diagnosis capabilities. Despite continuous advancements in temperature measurement technologies, real-time, rapid, and high-precision monitoring of FPGA surface temperature remains a central challenge in ensuring stable system operation, urgently requiring effective solutions. In this work, a fiber-optic temperature sensor for monitoring the surface temperature of an FPGA has been developed, featuring an upconversion luminescence-enhanced fiber microsphere structure consisting of upconversion nanoparticles (UCNPs) with polymethyl methacrylate (PMMA), ensuring high-precision temperature measurement capability. To investigate its sensing performance, the fiber-optic microsphere sensor was evaluated within the temperature range of 300-350 K using fluorescence intensity ratio (FIR) technology. The results revealed a peak relative sensitivity of 1.27% K^{-1} at 300 K and demonstrated a detection accuracy superior to 0.5°C. The fiber-optic sensor was positioned on an FPGA chip and monitored for temperature changes through multiple consecutive power-on and cooling cycles. Comparison with the FPGA board's built-in temperature sensor showed high consistency in operating temperatures. Notably, the fiber-optic sensor demonstrated superior resistance to external environmental interference. The results indicate that the developed sensor, from material design to device application, has great potential for precise and stable temperature monitoring in FPGA applications.

1. Introduction

Advancements in semiconductor process technology have ushered in profound transformations in chip design and fabrication. Notably, FPGA chips, exemplary programmable logic devices, have achieved remarkable high-density integration of millions of transistors and electronic components [1]. The quantity and complexity of circuits operating concurrently on a single chip have increased significantly with the improvement of integration density. When executing various tasks, substantial electrical energy is required by these circuits to drive the rapid switching of transistor states. As the operating frequency increases, i.e., the number of operations completed by circuit elements per unit time grows, power consumption is also dramatically surged [2–4].

This escalating power consumption exacerbates the chip's temperature issue, as a considerable amount of heat is generated and rapidly accumulated within a short time, leading to a sharp rise in chip temperature [5]. The internal electronic components and interconnect structures of the chip are subjected to immense pressure by the high-temperature environment, potentially resulting in performance degradation (such as increased latency and signal attenuation), as well as accelerating material aging and failure mechanisms, ultimately shortening the chip's lifespan [6].

Implementing effective thermal management is crucial for ensuring FPGA chips operate within their optimal temperature range, thereby enhancing their processing speed and efficiency. The temperature measurement methods for FPGAs encompass a variety of techniques ranging from external to internal, and from direct reading to indirect estimation [7,8]. Internal temperature sensors or analog-to-digital converters (ADCs) may necessitate the utilization of some resources (such as I/O pins or internal logic). Upon power loss, their internal circuitry and components cease to function, rendering them incapable of providing temperature data [9,10]. External temperature sensors like DS18B20, during their operation, can experience accuracy degradation due to the influence of ambient temperature fluctuations, leading to significant errors in measurement results [11]. As for traditional electronic sensors such as chip resistors and thermocouples, they may fall short of meeting monitoring requirements in certain extreme environments (e.g., high electromagnetic interference, corrosive environments) or specific application scenarios (e.g., confined spaces, rapid temperature measurement needs), resulting in inaccurate monitoring signals [5,7]. Fiber optic sensors (FOSs), with their excellent long-term stability, strong electromagnetic interference resistance, high-speed response, high sensitivity and accuracy, as well as remote monitoring capabilities, have demonstrated immense potential in the field of real-time thermal monitoring for complex electronic devices [12–14]. However, the accurate demodulation of temperature signals by FOSs in highly integrated electronic equipment is interfered with by the cross-sensitivity effect of microvibrations [15]. Consequently, designing and developing fiber optic sensors capable of simultaneously resisting electromagnetic and microvibration interference has become a crucial research direction and urgent need for enhancing chip thermal management performance and ensuring stable device operation.

In the application of FOSs for non-contact temperature measurement, the proportional optical thermometer excels in precise temperature measurements, unaffected by fluctuations in light source power and light loss [16]. Lanthanide ions (Ln^{3+}), renowned for their narrow and stable emission peaks stemming from the proximity of the 4f electron shell to the atomic nucleus and shielding from external influences, emerge as the preferred material in optical thermometry. Materials doped with trivalent Ln^{3+} have been demonstrated to possess remarkable fast response characteristics, unparalleled measurement accuracy, and superior spatial resolution capabilities, leveraging their unique fluorescence intensity ratio (FIR) technology [17–20]. Remarkably, the Er^{3+}/Yb^{3+} co-doping system is recognized/identified as a standout feature. The $4S_{3/2}$ and $^2H_{11/12}$ energy levels of Er^{3+}, due to their close proximity, form an ideal thermally coupled level pair with an energy gap $\Delta E \approx 800\,cm^{-1}$. Additionally, Yb^{3+} ions exhibit a substantial absorption cross-section at 980 nm, facilitating efficient energy transfer that enhances the upconversion (UC) fluorescence emission of Er^{3+} ions, thereby boosting the sensitivity and accuracy of temperature measurements [21,22]. $NaYF_4$, as a host material, significantly suppresses multi-phonon relaxation processes owing to its low phonon energy, becoming a pivotal factor in enhancing upconversion luminescence efficiency [23]. Core-shell structured $NaYF_4$: $Er^{3+}/Yb^{3+}@NaYF_4$ upconversion nanoparticles (UCNPs) have been proven their applicability in various temperature measurement studies [24–26]. Integrating UCNPs with polymers, particularly through manufacturing methods that avoid high-temperature processing, not only preserves the stability of UCNPs but also expands their functionality and application range by leveraging the properties of the polymer matrix [27,28]. In the realm of semiconductor microelectronics

design, real-time temperature monitoring and instant feedback for chips are paramount, enhancing circuit stability and prolonging the lifespan of electronic components. Thus, the development of fiber-optic temperature sensors utilizing UCNPs/polymer composites paves a promising avenue for future research, aiming to achieve efficient and precise temperature sensing capabilities.

In this work, β-NaYF$_4$:Er^{3+}/Yb^{3+}@NaYF$_4$ nanomaterials with a core-shell structure were synthesized through high-temperature thermal decomposition of lanthanide chloride precursors. Upon excitation with a 980 nm continuous-wave laser, bright green upconversion fluorescence was observed. The synthesized UCNPs were then mixed with polymethyl methacrylate (PMMA) and coated onto the surface of silica microspheres fabricated from single-mode fibers (SMFs), resulting in the successful preparation of a fluorescence intensity ratio (FIR)-based optical temperature sensor. At 300 K, the sensor exhibited a sensitivity of up to 1.27% K^{-1}, demonstrating the effectiveness of utilizing FIR analysis of fluorescence intensity for temperature monitoring. Through three-dimensional finite-difference time-domain (FDTD) numerical simulations, the mode field distribution within the PMMA-coated silica microspheres was investigated, revealing the presence of whispering gallery mode-like resonance for optical guidance. This low optical leakage enabled the nanoparticles doped within the PMMA shell to be efficiently triggered for upconversion effects by the 980 nm laser. Experimental results indicated that the upconversion fiber-optic microsphere sensor could be employed for real-time monitoring of surface temperatures on FPGA chips, achieving high-sensitivity real-time temperature measurements. This study have provided a novel and efficient solution for thermal monitoring of highly integrated electronic devices.

2. Materials and methods

2.1. Sample preparation

All chemical reagents were sourced from Aladdin (Beijing, China), and they were utilized directly without any additional purification steps: ammonium fluoride (NH$_4$F, > 98%), sodium hydroxide (NaOH, > 98%), 1- octadecene (ODE, 90%), oleic acid (OA, 90%), yttrium chloride (YCl$_3$, 99%), ytterbium chloride (YbCl$_3$, 99%), erbium chloride (ErCl$_3$, 99%), methanol, chloro-form, cyclohexane, ethanol, and polymethyl methacrylate (PMMA,M_W = 996 000).

Synthesis of NaYF$_4$:Er^{3+}/Yb^{3+}. The Er/Yb: NaYF$_4$ particles encapsulated with oleic acid (OA) were synthesized through a modified thermal decomposition method. Initially, methanol solutions of 0.1 M ErCl$_3$, 0.4 M YbCl$_3$, 1 M YCl$_3$, 0.5 M NaOH, and 0.5 M NH$_4$F were prepared. Then, OA (10 mL), ODE (15 mL), ErCl$_3$ solution (0.2 mL), YbCl$_3$ solution (0.45 mL), and YCl$_3$ solution (0.8 mL) were added to a 100 mL three-necked flask. The mixture was subjected to dehydration and methanol removal at 110°C for 10 minutes, followed by heating at 180°C for 40 minutes, and subsequently cooled to room temperature. Afterward, 5 mL of NaOH methanol solution and 8 mL of NH$_4$F methanol solution were added, and the mixture was stirred for 45 minutes. The reaction mixture was heated at 110°C for 15 minutes to remove residual methanol and water, and then rapidly heated to 300°C, where it was maintained for 1.5 hours. Subsequently, the solution was cooled to room temperature. The prepared nanocrystals were precipitated by adding ethanol, collected by centrifugation at 8000 rpm for 5 minutes, and washed several times with ethanol and methanol. The final product was dispersed in 10 mL of cyclohexane. Throughout the experimental process, argon gas was used to protect the reaction.

Synthesis of NaYF$_4$:Er^{3+}/Yb^{3+}@NaYF$_4$. Similar to the aforementioned synthesis process, OA (10 mL), ODE (15 mL), and YCl$_3$ solution (1 mL) were added to a 100 mL three-necked flask. The mixture was subjected to dehydration and methanol removal at 110°C for 10 minutes, followed by heating at 180°C for 40 minutes, and subsequently cooled to room temperature. Then, 5 mL of NaOH methanol solution, 8 mL of NH$_4$F methanol solution, and 10 mL of the previously synthesized Er/Yb: NaYF$_4$ cyclohexane solution from the first step were added, and the mixture was stirred for 45 minutes. The reaction mixture was heated at 110°C for 15 minutes to remove

residual methanol and water, and then rapidly heated to 300°C, where it was maintained for 1.5 hours. Subsequently, the solution was cooled to room temperature. The prepared nanocrystals were precipitated by adding ethanol, collected by centrifugation at 8000 rpm for 5 minutes, and washed several times with ethanol and methanol. The final product was dispersed in 10 mL of cyclohexane. Throughout the experimental process, argon gas was used to protect the reaction.

$NaYF_4$:Er^{3+}/Yb^{3+}@$NaYF_4$-PMMA composite and fiber-optic microsphere sensor preparation. The fixed standard single-mode fiber (SMF) was subjected to arc discharge through a fiber fusion splicer, and the fiber was gradually tapered through the tapering process. Subsequently, the fiber tip was secured on the manufacturing platform of a CO_2 laser, where the tapered fiber tip underwent infrared laser ablation to form an initial pure silica microsphere. 0.005 g of UCNPs were dispersed in 5 ml of cyclohexane solution through ultrasonic vibration. Separately, 0.5 g of PMMA was dissolved in 5 ml of chloroform solution. The UCNPs solution was mixed with the PMMA-chloroform solution and sonicated for 1 hour. The prepared silica microsphere was repeatedly immersed in the aforementioned mixed solution, during which the mixed solution gradually adhered and solidified on the surface of the silica microsphere through repeated dipping and evaporation processes. Finally, heating in an oven was performed to allow for the complete evaporation of chloroform and cyclohexane. This resulted in the fabrication of a smooth-surfaced upconversion microsphere optical fiber sensor. The manufacturing process can be found in Fig. 2(a).

2.2. Characterization

To characterize the samples, a variety of advanced material analysis techniques were employed. The crystalline phase structures of two types of nanoparticles were analyzed using X-ray diffraction (XRD, Cu Ka radiation) and high-resolution transmission electron microscopy (HRTEM). The microscopic morphology of the microsphere surface structures was observed with a field-emission scanning electron microscope (SEM). The morphology distribution and elemental composition of the UCNP/PMMA coating on the microsphere surface were inspected using transmission electron microscopy (TEM) and element mapping. For spectral analysis, a 980 nm laser (LWIRL980-7W, Laserwave) was utilized as the excitation source, and the resulting UC fluorescence emission spectra generated by the samples under excitation were precisely detected and recorded by a spectrometer (QEpro, Ocean Optics). Additionally, optical images were captured using an optical microscope equipped with a 10× objective lens (NA = 0.9, Olympus).

3. Results and discussion

The Yb^{3+}/Er^{3+} co-doped $NaYF_4$ material was synthesized *via* the decomposition of lanthanide chloride precursors in high-temperature organic solvents and surfactants. The TEM image of $NaYF_4$: Yb^{3+}/Er^{3+} shown in Fig. 1(a) distinctly showcases the regular hexagonal structure of the core-only UCNPs. Upon 100 measurements, the average size was ≈19.95 nm, with the size distribution presented in the inset of Fig. 1(a). Figure 1(b) and (c) exhibit the TEM images of $NaYF_4$: Er^{3+}/Yb^{3+}@$NaYF_4$ at different scales, indicating that the average length of the grown particles was ≈57.67 nm, and the width was ≈29.34 nm, with the size distribution illustrated in the inset of Fig. 1(b). As shown in the lower right inset of Fig. 1(c), HRTEM imaging analysis of a single UCNP reveals a *d*-spacing of ≈0.52 nm between adjacent lattice fringes. This spacing was found to match the characteristic peak of the (100) plane in β-$NaYF_4$ crystals when compared with the bottommost standard diffraction peak (PDF no. 16-0334) in the XRD pattern of Fig. 1(d). Figure 1(d) presents the XRD diffraction patterns of core-shell UCNPs (blue curve) and core-only UCNPs (red curve). The Er^{3+}/Yb^{3+} co-doped $NaYF_4$ crystals exhibit no significant shift in diffraction peak positions when compared to β-$NaYF_4$ crystals, which is attributed to the similar ionic radii of Er^{3+}, Yb^{3+}, and Y^{3+}. The enhanced diffraction peak intensity of the core-shell UCNPs indicates an improved crystallinity, suggesting a more ordered arrangement of atoms/ions

within the crystal lattice, with reduced defects and dislocations, favorable for enhancing optical properties. In the presence of abundant oleic acid, preferential passivation of the (100) facets occurs, promoting the longitudinal growth of nanoparticles. This results in the epitaxial growth of the shell layer tending to proceed along the *c*-axis, ultimately leading to the formation of nanorod morphologies [24,25].
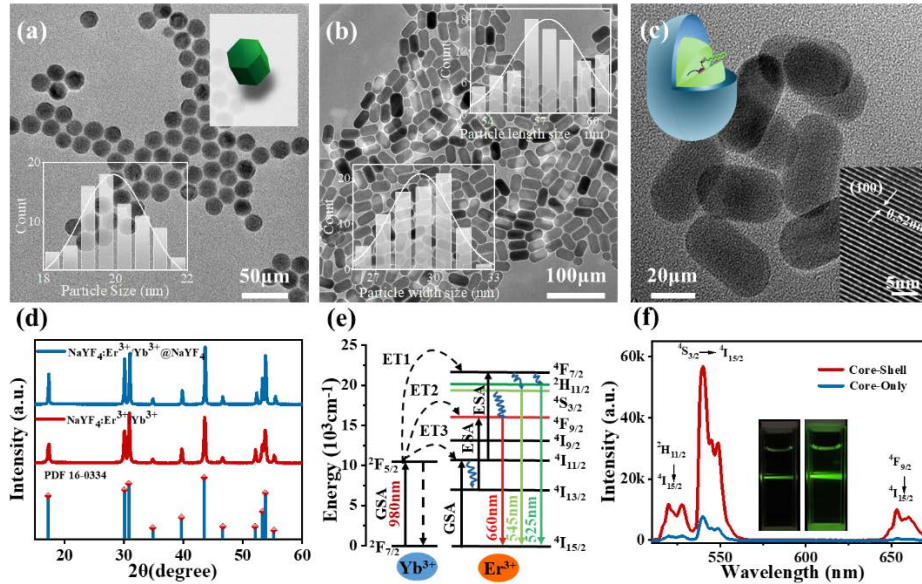
Fig. 1. (a) TEM image of $NaYF_4:Er^{3+}/Yb^{3+}$; (b and c) TEM image of $NaYF_4:Er^{3+}/Yb^{3+}@NaYF_4$ at different scales; (d) XRD patterns of Er^{3+}/Yb^{3+} co-doped $NaYF_4$ phosphors; (e) The structure diagram of $NaYF_4:Er^{3+}/Yb^{3+}@NaYF_4$ and its possible upconversion luminescence mechanisms; (f) The upconversion luminescence spectra of $NaYF_4:Er^{3+}/Yb^{3+}$ and $NaYF_4:Er^{3+}/Yb^{3+}@NaYF_4$. The Inset shows photographs of nanoparticles dispersed in a cyclohexane solution under 980 nm laser excitation.

The energy level transition process of core-shell UCNPs under 980 nm laser excitation was shown in Fig. 1(e). In the process, Yb^{3+} acts as a sensitizer, efficiently absorbing the 980 nm laser energy, causing the electrons in its $^2F_{7/2}$ energy level to transition to $^2F_{5/2}$. Subsequently, the energy is transferred to Er^{3+} via an energy transfer upconversion (ETU) process [29]. This energy transfer process significantly facilitates the excitation of Er^{3+}, leading to the emission of three characteristic emission bands, corresponding to the energy level transitions of $^2H_{11/12} \rightarrow {}^4I_{15/2}$, $^4S_{3/2} \rightarrow {}^4I_{15/2}$, and $^4F_{9/2} \rightarrow {}^4I_{15/2}$, respectively [26]. In the upconversion fluorescence spectra presented in Fig. 1(f), these transitions manifest distinctly in the spectra of both core-only UCNPs and core-shell UCNPs, specifically as prominent emission peaks of Er^{3+} at 525 nm, 545 nm, and 660 nm. The inset in Fig. 1(f) visually contrasts the luminescence performance of two types of nanocrystals, namely core-only UCNPs (left) and core-shell UCNPs (right), dispersed in cyclohexane solutions, both at a concentration of 1 mmol/mL. Under identical excitation power, the core-shell UCNPs solution exhibits a more intense green upconversion fluorescence, with notable enhancements of 8.3-fold and 9.4-fold, respectively, in the light intensities corresponding to the energy level transitions of $^2H_{11/2} \rightarrow {}^4I_{15/2}$ and $^4S_{3/2} \rightarrow {}^4I_{15/2}$. The superior fluorescence efficiency of Core-shell UCNPs compared to Core-only UCNPs is primarily attributed to their unique core-shell structure, specifically the role of the inert shell layer. This configuration effectively mitigates surface defects and quenching processes, optimizes energy transfer pathways within the crystal, thereby significantly enhancing luminescence efficiency and ensuring stronger

fluorescence output [30]. This advancement enables temperature sensors based on these crystals to exhibit higher sensitivity and precision in practical applications.

PMMA, owing to its exceptional transparency, outstanding refractive index (1.495) and dispersion properties, high heat resistance, good processability, and environmental friendliness, has emerged as an ideal material for the fabrication of optical devices and equipment [31]. Leveraging these advantages, a fiber-optic probe capable of receiving upconversion fluorescence has been developed by combining a mixed solution of UCNPs/PMMA with silica microspheres produced via optical fiber fusion tapering, with the specific process illustrated in Fig. 2(a). Figure 2(b) presents a microscopic image of the fabricated coated microspheres, where it can be observed that the microspheres exhibit good overall light transmission, a smooth and uniform surface, with a diameter of ≈70 μm. Upon excitation with a 980 nm laser, the surface of the microspheres displays bright green upconversion fluorescence, as shown in Fig. 2(c). Further inspection via SEM imagery (Fig. 2(d)) reveals that the microspheres possess perfect spherical boundaries and a smooth surface. Additionally, the TEM image in Fig. 2(e) elucidates the distribution of UCNPs within the PMMA. The TEM image indicates that the nanoparticles are relatively uniformly dispersed within the PMMA, albeit with the presence of localized clusters of varying sizes, which may be attributed to van der Waals forces [32] and electrostatic attraction effects among the nanoparticles. As depicted in Fig. 2(f–k), Na, Y, F, Er, and Yb elements have been successfully distributed within the PMMA layer on the surface of the optical fiber microspheres, signifying the effective incorporation of core-shell structured UCNPs into this layer and their tight bonding with the outer surface of the optical fiber microspheres.

Given the narrow energy gap between the $^2H_{11/2}$ and $^4S_{3/2}$ energy levels of Er^{3+} ($\Delta E \approx 800 \, cm^{-1}$), the electron population distribution within these thermally coupled levels was susceptible to temperature changes [33]. To comprehensively examine the temperature sensing properties of Er^{3+}/Yb^{3+} co-doped UCNPs/PMMA-based optical fiber probes, their upconversion emission spectra were recorded under varying external temperatures. The experimental setup designed for this study of photothermal performance was depicted in Fig. 3(a). Employing a 980 nm laser (LWIRL980-7W, Laserwave) as the pumping source, at a low power of 5 mW, the 980 nm light was transmitted along the optical fiber via a 2*1 coupler, ultimately exciting the core-shell UCNPs positioned at the fiber's terminal. Bright green upconversion fluorescence can be visually observed under a microscope, with a portion of the green emission signals propagating backward through the fiber, monitored by a high-performance fiber optic spectrometer (QEpro, Ocean Optics) for spectral analysis. The local temperature at the fiber probe was regulated by a thermostat (PG08, Murzider) with a temperature resolution of 0.1 K, which gradually heated up while allowing for real-time temperature readings. To ensure the safety and durability of the chip, spectral responses within a temperature range of 300 K to 350 K were recorded, as this range was considered suitable for the normal operation of the chip.

Figure 3(b) illustrates the temperature-dependent normalized spectrum of the sensor as the temperature increases from 300 K to 350 K, while the corresponding energy contours was depicted in Fig. 3(c). In comparison with Fig. 1(f), it was evident that the change in temperature did not cause a shift in the emission peak position. However, with the increase in temperature, the upconversion emission intensity at 545 nm gradually decreased, whereas the emission intensity at 525 nm slowly increased. This opposing variation in upconversion emission intensities was a direct result of the redistribution of electron populations between the $^2H_{11/2}$ and $^4S_{3/2}$ energy levels. Specifically, as the temperature rose, thermally excited electrons from the $^2H_{11/2}$ level (upper level) became more significantly occupied at the expense of those in the $^4S_{3/2}$ level (lower level). Consequently, the electron population distributions in these two adjacent energy levels, $^2H_{11/2}$ and $^4S_{3/2}$, strictly adhere to Boltzmann statistics, and their distribution states can be
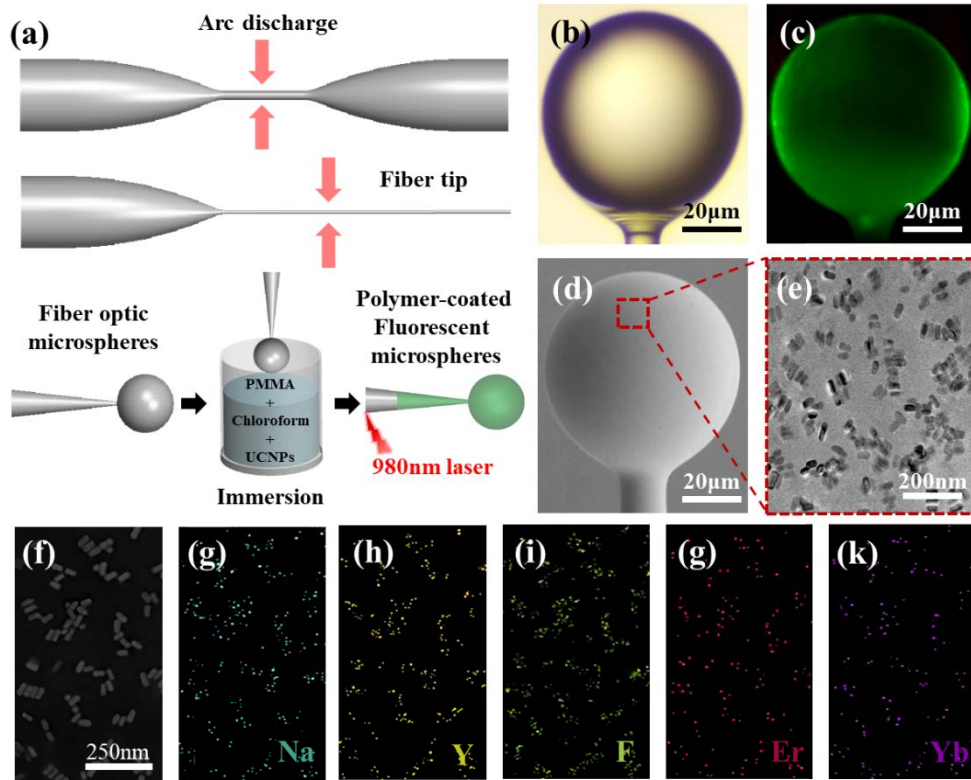
Fig. 2. (a) Manufacturing process of fiber-optic microsphere sensor; (b) microscope image of the optical probe; (c) Dark field microscopy images of optical probes excited by 980 nm laser; (d) SEM image of an optical fiber probe coated with $NaYF_4$:Er^{3+}/Yb^{3+}@$NaYF_4$/PMMA; (e) TEM micrographs of $NaYF_4$:Er^{3+}/Yb^{3+}@$NaYF_4$/ PMMA; (f-k) Elemental mapping images of $NaYF_4$:Er^{3+}/Yb^{3+}@$NaYF_4$/ PMMA compounds.

expressed as [34]:

$$\text{FIR} = \frac{I_H}{I_S} = C\exp\left(\frac{-\Delta E}{kT}\right) \tag{1}$$

herein, I_H represents the integral intensity within the wavelength range of 515–537 nm, corresponding to the transition from $^2H_{11/2}$ to $^4I_{15/2}$, while I_S represents the integral intensity within the wavelength range of 537–560 nm, corresponding to the transition from $^4S_{3/2}$ to $^4I_{15/2}$. Additionally, C is a constant, ΔE represents the energy difference between the thermal coupling energy levels $^2H_{11/2}$ and $^4S_{3/2}$, k denotes the Boltzmann constant, and T stands for absolute temperature. Figure 4(a) illustrates the dependence of the I_{525}/I_{545} ratio on temperature (T), and the relationship between this ratio and temperature can be well fitted using Eq. (1). The data points closely follow the fitted curve, exhibiting a high degree of goodness-of-fit, with a regression coefficient (R^2) reaching 0.993. Further analysis of the fitting results yields a value of 18.61 for C and 826.32 for ΔE, indicating an excellent match between ΔE and the thermally coupled energy level of Er^{3+} ions ($\approx 800\,cm^{-1}$), which further validates the rationality and accuracy of the experimental design.

In the practical application of optical temperature sensing materials, the temperature-dependent variation of FIR serves as a pivotal indicator for assessing their temperature sensing performance. To quantify this performance more precisely, two key parameters are introduced: the absolute
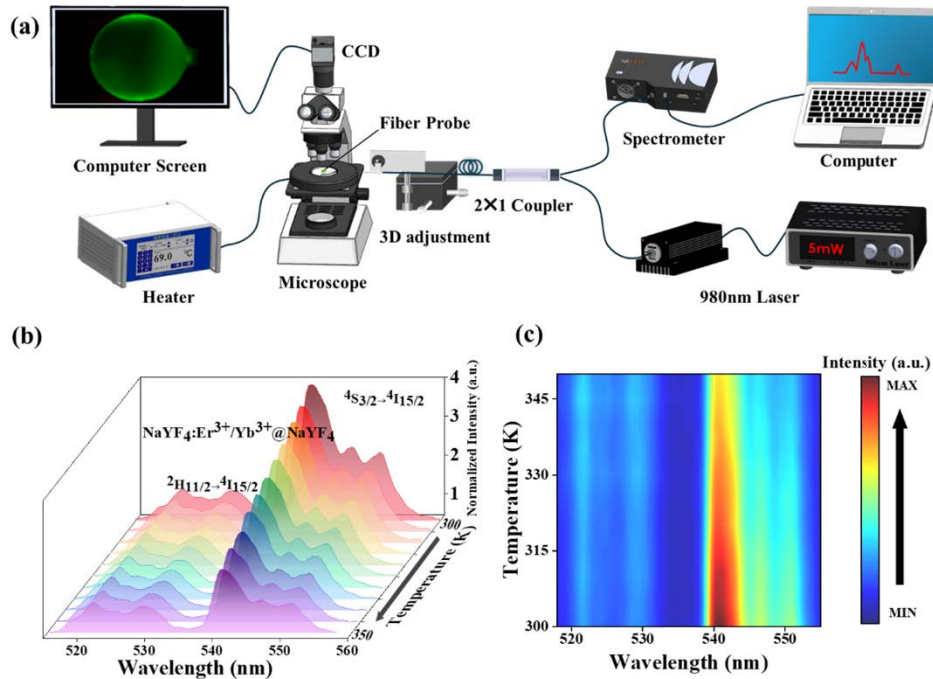
Fig. 3. (a) Schematic diagram of optical fiber temperature sensing device based on UCNPs/PMMA composite; (b) Temperature-dependent upconversion emission spectrum of the sensor; (c) Isolines of energy distribution.
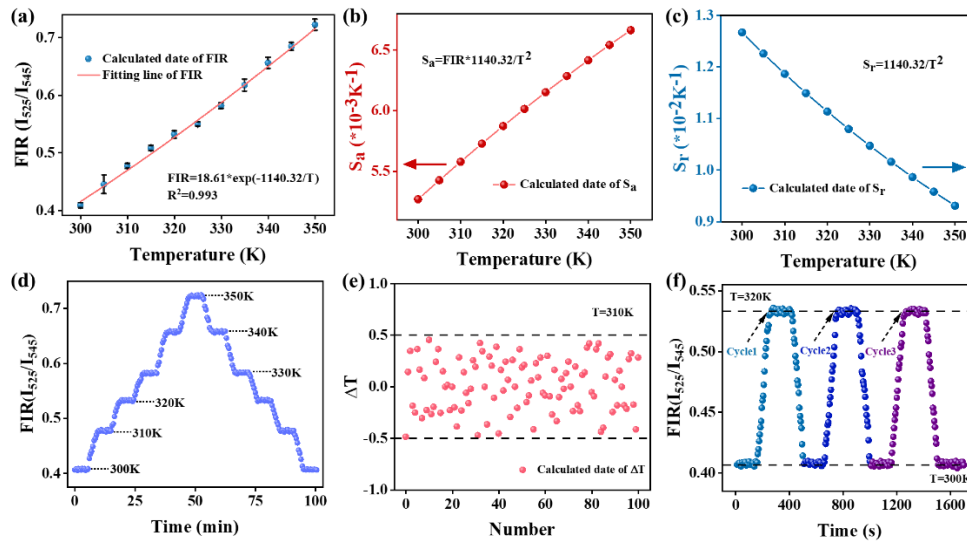
Fig. 4. (a) Linear fitting of FIR with temperature of FOSs; (b) The absolute sensitivity Sa versus temperature; (c) The relative sensitivity Sr versus temperature; (d) Response of the FOSs in the temperature cycle range; (e) The different ΔT values at 310 K; (f) Cycling test with a change in temperature within the range of 300 K–320 K.

sensitivity (S_a) and the relative sensitivity (S_r). S_a is defined as the absolute rate of change of FIR with respect to temperature, directly reflecting the sensitivity of the material to temperature variations. Specifically, a higher S_a value signifies a more pronounced variation of FIR with temperature, indicating stronger perception and response capabilities of the material to temperature changes. The calculations are detailed below [35]:

$$S_a = \frac{d\text{FIR}}{dT} = \text{FIR}\left(\frac{\Delta E}{kT^2}\right) \tag{2}$$

S_r is a normalized value based on the S_a, which further elucidates the relative proportional relationship between the rate of change of FIR and its current value.

$$S_r = \frac{1}{\text{FIR}}\frac{d\text{FIR}}{dT} = \frac{\Delta E}{kT^2} \tag{3}$$

Figure 4(b) and (c) exhibit the fitted curves of Sa and Sr, respectively, as a function of temperature within the range of 300-350 K. The plots indicate that the value of Sa increases with the elevation of ambient temperature, reaching a maximum of 0.67%K^{-1} at 350 K, whereas the value of Sr gradually decreases with increasing ambient temperature, achieving its highest sensitivity of 1.27%K^{-1} at 300 K. The enhanced upconversion emission characteristics exhibited by the core-shell structured fluorescent material are recognized as a crucial factor in enhancing optical detection sensitivity [29,36]. Table 1 compares the sensitivity performance of various upconversion materials in optical fiber temperature sensors. The sensor fabricated in this study outperforms some of the previously reported sensors in maximum relative sensitivity, highlighting its superior thermal sensing performance as well as the high standard of its design and fabrication processes. The temperature sensor was subjected to stepwise heating and cooling measurements with a temperature interval of 10 K, utilizing a temperature control device, and concurrently, the upconversion emission spectra were recorded and the FIR values were calculated. As depicted in Fig. 4(d), the FIR values increasd with the rise in temperature and reverted back to their original values when the temperature was reduced to the local initial temperature. Under conditions where the ambient temperature was stabilized at 310 K, 100 upconversion spectra were recorded, as shown in Fig. 4(e). The temperature values of all measurement points fluctuated around 310 K, indicating that continuous excitation at 5 mW power had no significant impact on the readings, with a detection limit within ±0.5°C. The intensity of fluorescence spectra is enhanced as the excitation power increases, while the temperature sensing performance based on FIR technology remains unaffected by power variations. The interference from excitation power fluctuations on sensing results can be effectively negated or disregarded by FIR technology, thus ensuring the accuracy and stability of temperature measurements. Subsequently, a multi-cycle heating-cooling experiment was conducted, as illustrated in Fig. 4(f). Within the temperature range of 300 K to 320 K, the sensor exhibited reversible and stable temperature responses during periodic thermal variations. The sensor exhibits extremely short response times during the heating and cooling processes. This characteristic indicates that real-time temperature changes can be tracked by the sensor, with no significant lag effect observed. These experimental results have collectively demonstrated the high reliability, repeatability, and precise measurement capabilities of the fabricated fiber-optic temperature sensor.

To ensure efficient upconversion luminescence of NaYF$_4$: Er^{3+}/Yb^{3+}@NaYF$_4$ nanoparticles triggered by 980 nm continuous-wave (CW) laser, a three-dimensional finite-difference time-domain (FDTD) numerical simulation was employed to analyze the modal field distribution within a silica microsphere coated with PMMA. A three-dimensional simulated core-shell structure with a diameter and shell thickness consistent with the experiment was drawn, and the refractive indices of air, PMMA shell, and silica core from the outside to the inside were set to 1, 1.495, and 1.45, respectively. The field distribution in the x-z and x-y planes of the microcavity is shown in

Table 1. Comparison of upconversion material-based optical fiber temperature sensors

Phosphor	$S_{max}(\%K^{-1})$	Working Range (K)	Ref.
$NaBi(WO_4)_2$: Er^{3+}/Yb^{3+}	1.24	298.15-373.15	[37]
$NaLuF_4$:$Yb^{3+}/Er^{3+}/Tm^{3+}$	0.77	300-600	[38]
Al_2O_3:Yb^{3+}/Er^{3+}	0.51	295-973	[39]
$NaYF_4$: Er^{3+}/Yb^{3+}	1.13	303-483	[40]
YF_4:$Yb^{3+}/Er^{3+}/Tm^{3+}$	1.01	293-563	[41]
$NaYF_4$: Er^{3+}/Yb^{3+} @$NaYF_4$	1.27	300-350	This work

Fig. 5(a) and (b), and the results indicate that the majority of the energy is distributed on the inner surface of the PMMA shell, resulting in light guidance similar to the resonant mode of the whispering gallery mode (WGM). Figure 5(c) presents the radially normalized field intensity distribution image along the x-z plane. This low light leakage enables the nanoparticles doped inside the PMMA shell to be efficiently triggered by the 980 nm laser for up-conversion effect. To investigate the effect of microsphere diameter on FIR, UCNPs/PMMA-coated silica microspheres with diameters of 65 μm, 87 μm, and 105 μm were fabricated using the same process as previously employed, and their optical fiber sensing performance was tested within the temperature range of 300-350 K. Under identical experimental conditions and excitation powers, the upconversion fluorescence spectra of fluorescent microsphere sensors with different diameters were measured. As the diameter of the microspheres increased, a notable trend of enhanced fluorescence spectrum intensity was observed. This was primarily attributed to the increased microsphere diameter leading to an enlarged cone region size, which in turn reduced optical transmission losses and intensified the intensity of the backward-propagating green fluorescence signal. Figure 5(d-f) presents the fitting curves of FIR versus temperature, yielding constants C of 18.25, 18.52, and 18.55, respectively, with corresponding energy level differences ΔE of 822.09 cm^{-1}, 825.17 cm^{-1}, and 823.70 cm^{-1}. These results are similar to those obtained from the fitting data analysis of previously prepared optical fiber probe experiments (Fig. 4(a)), indicating strong reproducibility in the fabrication method and data acquisition. Upon analysis of the fitting curves between the FIR values and temperatures for microsphere sensors of various diameters, it was found that despite significant differences in spectral intensity, the fitting curves between the FIR values and temperatures maintained a high degree of consistency.

The highly consistent sensing data is attributed to the uniformity of temperature-sensitive materials within the same batch [34] and the robustness of the fluorescence intensity ratio (FIR) technique against disturbances, enabling the sensors to exhibit comparable sensing characteristics within the specified temperature range. Compared to the sensors traditionally based on Fiber Bragg Grating (FBG) and Fabry-Pérot (FP) interference techniques, which highly relied on the monitoring of overall spectral fluctuations, the sensors introduced in this study, based on FIR technology, exhibited significant advantages. Their core temperature measurement mechanism depended on the ratio of characteristic fluorescence peak intensities (I_{525}/I_{545}) of Er^{3+} ions at wavelengths of 525 nm and 545 nm, rather than changes in overall spectral intensity. This unique design endowed the sensors with natural resistance to overall spectral fluctuations induced by external environmental changes, particularly vibrations. By accurately calculating the ratio of dual-wavelength fluorescence intensities, FIR technology effectively mitigated the impact of common-mode interference, thereby greatly enhancing the accuracy and reliability of temperature measurements.

To evaluate the performance of the designed fiber-optic temperature sensor in practical thermal monitoring applications, the AX7020 Xilinx FPGA development board was selected as the test subject. During operation, particularly under heavy load conditions, the central region of the chip would experience notable heat accumulation [3,5]. To ensure measurement accuracy, the
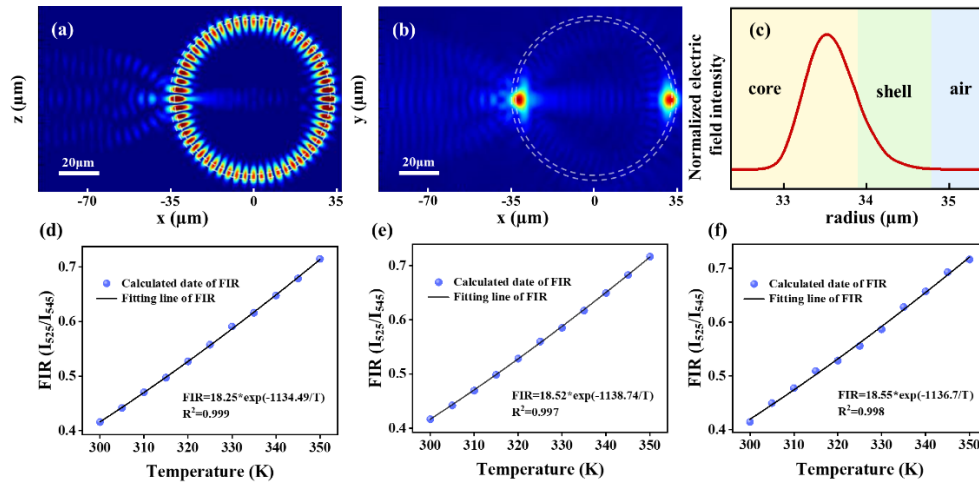
Fig. 5. (a and b) The field distribution in the x-z and x-y planes of the microspheres; (c) The radially normalized field intensity distribution image along the x-z plane; (d-f) Fitting curves of FIR values and temperature for microspheres with different diameters.

location of the hot spot was predetermined, and with the aid of a high-precision three-dimensional displacement platform (with positioning accuracy of ±0.1μm), the optical fiber probe was precisely fixed at the center of the FPGA surface, thereby ensuring precise spatial positioning and stable optical coupling between the sensor and the FPGA chip. Consequently, the fiber-optic probe was affixed to the center of the FPGA surface, as depicted in the physical image shown on the left of Fig. 6(a). The upper right section of Fig. 6(a) presentsed an image illustrating the variation in the probe's fluorescence intensity as the surface temperature changes, with the probe positioned at the center of the FPGA under 980 nm laser excitation. Below this image was the corresponding upconversion fluorescence spectrum, which reveals a gradual decrease in fluorescence intensity and spectral strength as the temperature rises. This phenomenon underscored the feasibility of utilizing the designed probe for real-time feedback of the chip surface temperature.

The surface of the FPGA chip underwent real-time and periodic temperature monitoring. Upon powering on the board, the FPGA continuously generates heat due to the flow of current [7]. Every second, an upconversion spectrum was recorded by the system, and the corresponding FIR value was calculated. Simultaneously, the LM75 sensing module, integrated into the AX7020 Xilinx board, was used to monitor the internal temperature of the chip after powering on the FPGA board and loading the programmed program. The temperature value in the board register was read and transmitted back to the upper computer for display through the allocated I/O pins via serial communication. After several consecutive cycles of repeated power-on and cooling of the board, the detection results of the chip heating process were shown in Fig. 6(b), where the recorded operating temperature values of the chip remain essentially consistent.

The temperature trends monitored by the two sensors during the FPGA's power-on process were completely identical, indirectly validating the accuracy of the optical temperature measurement method. However, upon power disconnection, the LM75 temperature sensor module ceased operation, unable to continue tracking the chip's temperature (as indicated by the blue dashed region in Fig. 6(b)), whereas the optical fiber temperature sensor remained unaffected, continuously providing real-time chip temperature data. Notably, Fig. 6(b) also revealed an average temperature difference of approximately 3.8°C between the two sensors, attributed to the chip packaging effect. Further detailed analysis of the first two plots in the upper part of Fig. 6(b) clearly showed that the temperature data recorded by the optical fiber sensor (red curve) exhibits less fluctuation compared
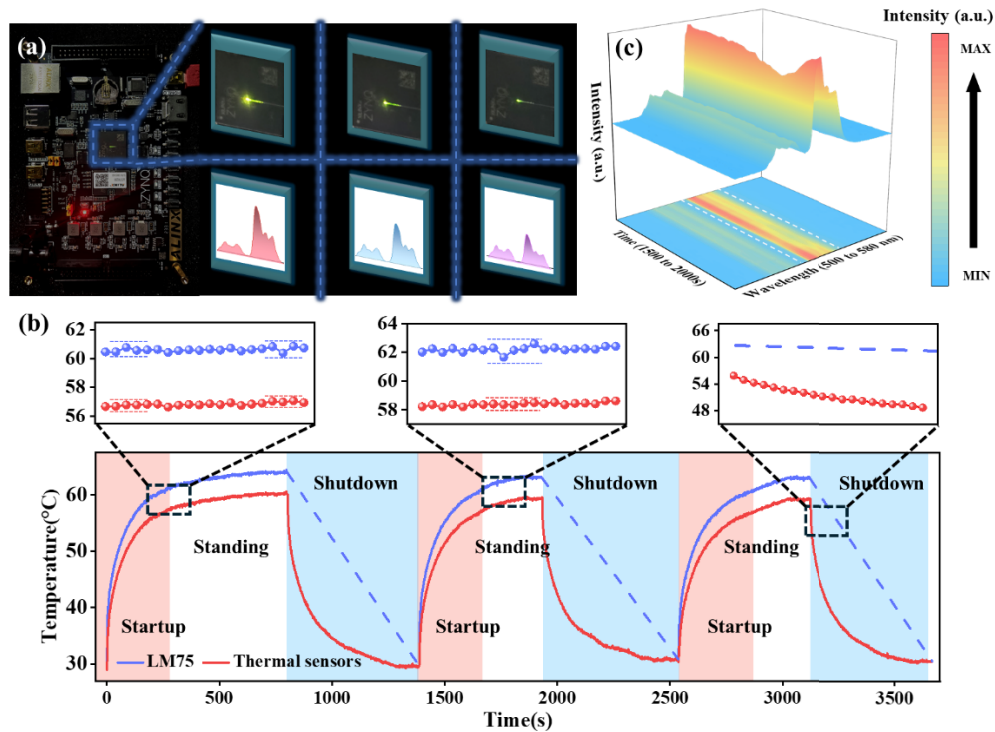
Fig. 6. (a) Left: Physical image of the FPGA chip. Right: Demonstration of temperature-dependent variation in upconversion fluorescence intensity from the optical fiber sensor positioned on the chip surface, along with their corresponding spectra; (b) Temperature time relationship diagram during three consecutive cycles of repeated power on cooling. The above image is a magnified partial view of the temperature curve; (c) Real time spectral changes from 1500s to 2000s.

to the LM75 temperature sensor module (blue curve), highlighting the superior performance of the optical fiber sensor in resisting external environmental interference. Additionally, the last plot in the upper part of Fig. 6(b) visually demonstrated that continuous temperature monitoring was maintained through the optical fiber sensor even when the power was cut off. The real-time upconversion fluorescence spectrum over the time period from 1500s to 2000s was presented in Fig. 6(c). The optical temperature measurement technique utilizing an external pump source focuses on detecting temperature changes in the excitation region. In contrast, the optical fiber sensor uniquely excels in accurately measuring the temperature at the tangent point between the microsphere and the chip surface, achieving high-precision temperature monitoring with micrometer-level spatial resolution [26,42]. This series of experimental results not only proves the efficient, reliable, and real-time thermal monitoring capabilities of the upconversion optical fiber microsphere sensor in highly integrated electronic devices but also offers a novel and powerful temperature measurement approach for future chip design and development.

4. Conclusions

In summary, the core-shell structured β-NaYF$_4$:Er^{3+}/Yb^{3+}@NaYF$_4$ nanoparticles were successfully synthesized via thermal decomposition, exhibiting bright upconversion fluorescence under 980 nm laser excitation. Analysis has revealed the upconversion emission mechanism of the

Er^{3+}–Yb^{3+} pair within the UCNPs. A fiber-optic temperature sensor, composed of silica microspheres integrated with UCNPs/PMMA, was fabricated. This sensor utilized whispering gallery mode resonance for optical guidance, enabling efficient triggering of the upconversion effect by 980 nm laser light. Within the temperature range of 300-350 K, the performance of the fiber-optic microsphere sensor was evaluated using FIR technology. The results indicated that the sensor achieves a high sensitivity of $1.27\%K^{-1}$ at 300 K, with a detection accuracy better than 0.5°C, demonstrating good repeatability and stability. When placed on the surface of an FPGA chip, the sensor successfully realized real-time thermal monitoring during multiple consecutive power-on and cooling cycles. In applied research, the fiber-optic sensor has demonstrated exceptional resistance to external environmental interference, along with advantages such as small size, high sensitivity, and strong electromagnetic interference resistance. The upconversion fiber-optic microsphere sensor in this study has demonstrated exceptional performance in monitoring the temperature of integrated circuits and holds promising potential to become a reliable temperature measurement tool for ensuring the operational safety of miniature electronic devices in the future.

Disclosures. The authors declare no conflicts of interests.

Data availability. Data underlying the results presented in this paper are not publicly available at this time but may be obtained from the authors upon reasonable request.

References

1. Z. Abid, M. Liu, and W. Wang, "3D integration of CMOL structures for FPGA applications," IEEE Trans. Comput. **60**(4), 463–471 (2011).
2. N. Grover and M. K. Soni, "Reduction of power consumption in FPGAs-an overview," IJIEEB **4**(5), 50–69 (2012).
3. M. Vaithianathan, M. Patil, S. F. Ng, *et al.*, "Energy-Efficient FPGA Design for Wearable and Implantable Devices," ESP-IJAST **2**(2), 37–51 (2024).
4. E. Antolak and A. Pułka, "Power Consumption Prediction in Real-Time Multitasking Systems," Electronics **13**(7), 1347 (2024).
5. W. Yu, S. Feng, Y. Zhang, *et al.*, "Temperature distribution measurement based on field-programmable gate array embedded ring oscillators," Solid-State Electron. **158**, 16–21 (2019).
6. A. A. Almubarak, "The effects of heat on electronic components," Int. J. Eng. Res. Appl **07**(5), 52–57 (2017).
7. Y. Luo, J. C. Zhao, A. Aggarwal, *et al.*, "Thermal management for fpga nodes in hpc systems," ACM Trans. Des. Autom. Electron. Syst **26**(2), 1–17 (2021).
8. A. Oukaira, O. Ettahri, M. Tabaa, *et al.*, "Simulation, validation and FPGA implementation of a ring oscillator sensor for thermal management and monitoring," Procedia Comput **155**(4), 83–88 (2019).
9. G. Payá-Vayá, C. Bartels, and H. Blume, "Small footprint synthesizable temperature sensor for FPGA devices," J Syst Architect **76**(4), 28–38 (2017).
10. J. D. E. Castillo, E. Canto-Navarro, and E. Vidal-Idiarte, "Design and implementation of scalable and parametrizable analog-to-digital converter on FPGA," Electronics **11**(3), 447 (2022).
11. L. Su, "Design of RF Heat Therapy System Based on DS18B20 and FPGA," Sens. Transducers **178**(9), 140 (2014).
12. V. R. Mamidi, S. Kamineni, L. S. P. Ravinuthala, *et al.*, "High-temperature measurement using fiber Bragg grating sensor accompanied by a low-cost detection system," J. Appl. Remote. Sens. **9**(1), 094098 (2015).
13. A. Oukaira, A. Z. Benelhaouare, E. Kengne, *et al.*, "FPGA-embedded smart monitoring system for irrigation decisions based on soil moisture and temperature sensors," Agronomy **11**(9), 1881 (2021).
14. S. Zhao, Q. Liu, J. Chen, *et al.*, "Resonant fiber-optic strain and temperature sensor achieving thermal-noise-limit resolution," Opt. Express **29**(2), 1870–1878 (2021).
15. D. Kang, H. Y. Kim, and D. H. Kim, "Enhancing thermal reliability of fiber-optic sensors for bio-inspired applications at ultra-high temperatures," SMS **23**(7), 074012 (2014).
16. C. Wang, Y. Jin, R. Zhang, *et al.*, "A review and outlook of ratiometric optical thermometer based on thermally coupled levels and non-thermally coupled levels," J. Alloy. Compd. **894**, 162494 (2022).
17. G. Baffou, P. Bon, J. Savatier, *et al.*, "Thermal imaging of nanostructures by quantitative optical phase Analysis," ACS Nano **6**(3), 2452–2458 (2012).
18. S. A. Wade, S. F. Collins, and G. W. Baxter, "Fluorescenceintensity ratio technique for optical fiber point temperature sensing," J. Appl. Phys. **94**(8), 4743–4756 (2003).
19. C. D. Brites, P. P. Lima, N. J. Silva, *et al.*, "Thermometry at the nanoscale," Nanoscale **4**(16), 4799–4829 (2012).
20. C. Zhang, J. Lu, N. Jin, *et al.*, "Plasmon-driven rapid in situ formation of luminescence single crystal nanoparticle," Small **15**(34), 1901286.1 (2019).
21. L. T. K. Giang, K. Trejgis, L. Marciniak, *et al.*, "Fabrication and characterization of up-converting β-$NaYF_4$:Er^{3+}, Yb^{3+}@$NaYF_4$ core–shell nanoparticles for temperature sensing applications," Sci. Rep. **10**(1), 14672 (2020).

22. K. Yang, R. Xu, Q. Meng, *et al.*, "Er^{3+}/Yb^{3+} co-doped TeO$_2$–ZnO–ZnF$_2$–La$_2$O$_3$ glass with a high fluorescence intensity ratio for an all-fiber temperature sensor," J. Lumin. **222**(34), 117145 (2020).

23. W. Gao, Z. Sun, Q. Han, *et al.*, "Enhancing upconversion emission of Er^{3+} in single β-NaYF$_4$ microrod through constructing different inert and active shells with doping Yb^{3+} ions," J. Alloys Compd. **857**(16), 157578 (2021).

24. H. Li, F. Wei, Y. Li, *et al.*, "Optical fiber sensor based on upconversion nanoparticles for internal temperature monitoring of Li-ion batteries," J. Mater. Chem. C **9**(41), 14757–14765 (2021).

25. Q. Guo, J. Wu, Y. Yang, *et al.*, "High performance perovskite solar cells based on β-NaYF$_4$: Yb^{3+}/Er^{3+}/Sc^{3+}@ NaYF$_4$ core-shell upconversion nanoparticles," J. Power Sources **426**(3), 178–187 (2019).

26. H. Li, M. Yu, J. Dai, *et al.*, "Upconversion Nanoparticle-Based Fluorescent Film for Distributed Temperature Monitoring of Mobile Phones' Integrated Chips," Nanomaterials **13**(11), 1704 (2023).

27. M. K. Shahzad, Y. Zhang, L. Cui, *et al.*, "Dispersing upconversion nanocrystals in PMMA microfiber: a novel methodology for temperature sensing," RSC Adv. **8**(35), 19362–19368 (2018).

28. J. Guo, B. Zhou, C. Yang, *et al.*, "Stretchable and upconversion-luminescent polymeric optical sensor for wearable multifunctional sensing," Opt. Lett. **44**(23), 5747–5750 (2019).

29. L. Liu, F. Qin, H. Zhao, *et al.*, "Shell thickness dependence of upconversion luminescence of β-NaYF$_4$: Yb, Er/β-NaYF$_4$ core-shell nanocrystals," Opt. Lett. **38**(12), 2101–2103 (2013).

30. L. Liu, D. Yan, L. Xu, *et al.*, "Intense and color-tunable upconversion through 980 and 1530 nm excitations," J. Lumin. **224**(12), 117306 (2020).

31. H. M. Zidan and M. Abu-Elnader, "Structural and optical properties of pure PMMA and metal chloride-doped PMMA films," Phys. Rev., B Condens. Matter **355**(1-4), 308–317 (2005).

32. Y. Bao, Q. A. N. Luu, Y. Zhao, *et al.*, "Upconversion polymeric nanofibers containing lanthanide-doped nanoparticles via electrospinning," Nanoscale **4**(23), 7369–7375 (2012).

33. G. Xiang, Q. Xia, X. Liu, *et al.*, "Optical thermometry based on the thermally coupled energy levels of Er^{3+} in upconversion materials," Dalton Trans. **49**(47), 17115–17120 (2020).

34. H. Zhang, J. Ye, X. Wang, *et al.*, "Highly reliable all-fiber temperature sensor based on the fluorescence intensity ratio (FIR) technique in Er^{3+}/Yb^{3+} co-doped NaYF$_4$ phosphors," J. Mater. Chem. C **7**(48), 15269–15275 (2019).

35. H. Zhang, S. Zhao, X. Wang, *et al.*, "The enhanced photoluminescence and temperature sensing performance in rare earth doped SrMoO$_4$ phosphors by aliovalent doping: from material design to device applications," J. Mater. Chem. C **7**(47), 15007–15013 (2019).

36. H. Tuxun, Z. Cai, M. Ji, *et al.*, "Controlling and probing heat generation in an optical heater system," Nanophotonics **11**(5), 979–986 (2022).

37. J. Gao, X. Ren, K. Yang, *et al.*, "Detection of hydrogen concentration based on an all-fiber fluorescence intensity ratio optical thermometer with Er^{3+}/Yb^{3+} codoped NaBi(WO$_4$)$_2$ phosphors," Optik **242**, 167280 (2021).

38. H. Lu, H. Hao, G. Shi, *et al.*, "Optical temperature sensing in β-NaLuF$_4$: Yb^{3+}/Er^{3+}/Tm^{3+} based on thermal, quasi-thermal and non-thermal coupling levels," RSC Adv. **6**(60), 55307–55311 (2016).

39. B. Dong, D. P. Liu, X. J. Wang, *et al.*, "Optical thermometry through infrared excited green upconversion emissions in Er^{3+}–Yb^{3+} codoped Al$_2$O$_3$," Appl. Phys. Lett. **90**(18), 181117 (2007).

40. L. Li, F. Qin, Y. Zhou, *et al.*, "Temperature sensing based on the ^{4}F$_{7/2}$/^{4}S$_{3/2}$– ^{4}I$_{15/2}$ upconversion luminescence intensity ratio in NaYF$_4$: Er^{3+}/Yb^{3+} nanocrystals," J. Lumin. **206**, 335–341 (2019).

41. D. Chen, S. Liu, X. Li, *et al.*, "Upconverting luminescence based dual-modal temperature sensing for Yb^{3+}/Er^{3+}/Tm^{3+}: YF$_3$ nanocrystals embedded glass ceramic," J. Eur. Ceram. Soc. **37**(15), 4939–4945 (2017).

42. T. Cheng, W. Liu, D. Song, *et al.*, "A compact fluorescent probe for real-time thermal monitoring of chips," J. Lightwave Technol. **40**(18), 6288–6295 (2022).